

Light emission from multiple self-trapped excitons in one-dimensional Ag-based ternary halides

Jiahao Xie(颉家豪), Zewei Li(李泽唯), Shengqiao Wang(王晟侨), and Lijun Zhang(张立军)

Citation: Chin. Phys. B, 2024, 33 (**11**): 117102. DOI: 10.1088/1674-1056/ad7e9c
Journal homepage: http://cpb.iphy.ac.cn; http://iopscience.iop.org/cpb

What follows is a list of articles you may be interested in

Near-field radiative heat transfer between nanoporous GaN films

Xiaozheng Han(韩晓政), Jihong Zhang(张纪红), Haotuo Liu(刘皓佗), Xiaohu Wu(吴小虎), and Huiwen Leng(冷惠文)

Chin. Phys. B, 2024, 33 (**4**): 047801. DOI: 10.1088/1674-1056/ad09a9

Effect of thickness of antimony selenide film on its photoelectric properties and microstructure

Xin-Li Liu(刘欣丽), Yue-Fei Weng(翁月飞), Ning Mao(毛宁), Pei-Qing Zhang(张培晴), Chang-Gui Lin(林常规), Xiang Shen(沈祥), Shi-Xun Dai(戴世勋), and Bao-An Song(宋宝安)

Chin. Phys. B, 2023, 32 (**2**): 027802. DOI: 10.1088/1674-1056/ac8724

Faraday rotations, ellipticity, and circular dichroism in magneto-optical spectrum of moiré superlattices

J A Crosse and Pilkyung Moon

Chin. Phys. B, 2021, 30 (**7**): 077803. DOI: 10.1088/1674-1056/ac051f

Effect of disorder on exciton dissociation in conjugated polymers

Yuwen Feng(冯誉雯), Hui Zhao(赵晖), Yuguang Chen(陈宇光), Yonghong Yan(鄢永红)

Chin. Phys. B, 2017, 26 (**10**): 107103. DOI: 10.1088/1674-1056/26/10/107103

Crossover of large to small radius polaron in ionic crystals

M I Umo

Chin. Phys. B, 2016, 25 (**11**): 117104. DOI: 10.1088/1674-1056/25/11/117104

DATA PAPER

Light emission from multiple self-trapped excitons in one-dimensional Ag-based ternary halides

Jiahao Xie(颉家豪)[†], Zewei Li(李泽唯)[†], Shengqiao Wang(王晟侨), and Lijun Zhang(张立军)[‡]

State Key Laboratory of Integrated Optoelectronics, Key Laboratory of Automobile Materials of MOE, Key Laboratory of Material Simulation Methods & Software of MOE, School of Materials Science and Engineering, Jilin University, Changchun 130000, *China*

(Received 17 August 2024; revised manuscript received 7 September 2024; accepted manuscript online 24 September 2024)

Ternary metal halides based on Cu(I) and Ag(I) have attracted intensive attention in optoelectronic applications due to their excellent luminescent properties, low toxicity, and robust stability. While the self-trapped excitons (STEs) emission mechanisms of Cu(I) halides are well understood, the STEs in Ag(I) halides remain less thoroughly explored. This study explores the STE emission efficiency within the A_2AgX_3 (A = Rb, Cs; X = Cl, Br, I) system by identifying three distinct STE states in each material and calculating their configuration coordinate diagrams. We find that the STE emission efficiency in this system is mainly determined by STE stability and influenced by self-trapping and quenching barriers. Moreover, we investigate the impact of structural compactness on emission efficiency and find that the excessive electron–phonon coupling in this system can be reduced by increasing the structural compactness. The atomic packing factor is identified as a low-cost and effective descriptor for predicting STE emission efficiency in both Cs_2AgX_3 and Rb_2AgX_3 systems. These findings can deepen our understanding of STE behavior in metal halide materials and offer valuable insights for the design of efficient STE luminescent materials. The datasets presented in this paper are openly available in Science Data Bank at https://doi.org/10.57760/sciencedb.12094.

Keywords: self-trapped exciton, Ag-based ternary halides, configuration coordinate diagrams, emission efficiency

PACS: 71.38.Ht, 78.20.Bh, 78.55.Hx **DOI:** 10.1088/1674-1056/ad7e9c

1. Introduction

All inorganic ternary metal halides based on monovalent ions of the IB elements, i.e., Cu(I) and Ag(I), are noted for their superior luminescent properties, low toxicity, cost-effectiveness, and high stability, making them prominent in optoelectronic applications.[1–6] Among them, Cu(I) halides, forming 1D or 0D structures, exhibit highly efficient self-trapped exciton (STE) luminescence, suitable for light-emitting diodes (LEDs) and ray detection.[7–14] Though Ag(I) halides generally have lower emission efficiency than Cu(I) halides, they offer stronger compositional modulation of luminescence properties and broader spectral coverage.[3,4] Additionally, Ag(I) halides exhibit superior stability due to better oxidation resistance, which is crucial for applications.[15–17] Ag(I) ternary metal halides, forming 2D or 1D structures, can be classified into $CsAgX_2$,[3,17] $CsAg_2I_3$,[18] and A_2AgX_3.[3,4,19] Among them, the A_2AgX_3 (A = Rb, Cs; X = Cl, Br, I) system with 1D structures, as shown in Figs. 1(a) and 1(b), stands out for its flexible composition and adjustable luminescence, covering nearly the entire visible spectrum from violet to red.[3–6,15,16,20,21] In single crystals of such materials, fast decay time in the nanosecond range and minimal self-absorption due to large Stokes shifts are commonly found, making them excellent for x-ray detection, especially when doped with small amounts of Cu(I) ions.[5,6,15,22,23]

However, despite a broader spectral range and abundant luminescence modulation methods, the atomistic understanding of STEs in Ag(I) halides remains insufficient. Kumar *et al.* investigated the composition-dependent luminescence properties of the A_2AgX_3 system and calculated the STE excitation and luminescence energies.[4] They found significant discrepancies with experimental measurements and attributed the luminescence source to defect-bound excitons (DBEs). Zhang *et al.* conducted theoretical calculations of STE and DBE in Rb_2AgBr_3, finding the STE localized within a $[AgBr_4]$ tetrahedron with an Ag atom distorted perpendicular to the 1D chain, while the Br vacancy DBE exhibited an excited-state structure with two closely approached Ag atoms.[5] Their STE calculations also diverged significantly from experimental results. In Cu(I) halides $CsCu_2X_3$ (X = Cl, Br, I), which also feature a 1D structure, Du identified three distinct STE states for each material and explained the luminescence energy redshift trend from $CsCu_2Cl_3$ to $CsCu_2I_3$.[24] This suggests a potentially rich STE landscape in 1D metal halides, which remains unexplored in Ag(I) halides.

Another important yet complex question is why different metal halides exhibit varying photoluminescence quantum

[†]These authors contributed equally to this work.

[‡]Corresponding author. E-mail: lijun_zhang@jlu.edu.cn

© 2024 Chinese Physical Society and IOP Publishing Ltd

yield (PLQY). For instance, in 1D Ag(I) halides, Rb_2AgCl_3 has a PLQY of 60%,[6] whereas Rb_2AgI_3 has less than 1%.[4] Understanding and predicting STE emission efficiency are complex as it requires not only an accurate description of the STE state but also consideration of the competition with other recombination processes, including non-radiative and free exciton (FE) recombination. There are experimental techniques, such as applying pressure, that can regulate the STE emission efficiency and provide deeper insights.[25–29] The one-dimensional configuration coordinate diagram (CCD) is an effective theoretical framework for describing the luminescence process of localized states.[30] It depicts the variation of ground-state and excited-state energies along the deformation path between the ground-state and excited-state equilibrium positions. A typical CCD of STE includes three potential energy surfaces (PESs): the ground state, the FE state, and the STE state, as illustrated in Fig. 1(c). After identifying the stable or metastable STE state, the three key energies, FE energy (E_{free}), STE energy (E_{STE}), and the ground-state energy corresponding to the deformed STE structure (E_{deform}), can be obtained, allowing for the calculation of excitation energy ($E_{\text{exc}} = E_{\text{free}}$), emission energy ($E_{\text{PL}} = E_{\text{STE}} - E_{\text{deform}}$), and self-trapping energy ($E_{\text{trap}} = E_{\text{free}} - E_{\text{STE}}$). The energies of intersection points between PESs are critical for understanding transitions between different states. They determine the energy barriers for the transition processes between states, namely, the self-trapping barrier ($E_{\text{barrier}} = E_{\text{trans}} - E_{\text{free}}$) for the transition from FE to STE and the luminescence quenching barrier ($E_{\text{quench}} = E_{\text{cross}} - E_{\text{STE}}$) for the non-radiative return from STE to the ground state through the PESs crossing point. The rates of these processes critically affect the efficiency of STE emission. A lower self-trapping barrier (E_{barrier}) favors the formation of the STE state and enhances the emission efficiency, while a higher quenching barrier (E_{quench}) inhibits non-radiative recombination and improves the STE emission as well.[31,32]

However, relevant studies are still limited for metal halide materials. CCD calculations for low-dimensional Cu(I) halides such as $Cs_3Cu_2I_5$[33] and $CsCu_2I_3$[34] have revealed very low or even non-existent self-trapping barriers, explaining their high emission efficiency. Besides, CCD calculations for different STE states in 2D hybrid perovskites have explained the origin of STE luminescence[35] and the phenomenon of pressure-induced enhancement of STE emissions.[28] Yet, no studies have rationalized the differences in emission efficiency across various materials based on CCDs. In this study, we explore the origin of varying STE emission efficiencies in the A_2AgX_3 (A = Rb, Cs; X = Cl, Br, I) system by identifying three unique STEs in each material and calculating their CCDs. We find that the emission efficiencies are primarily determined by STE stability and are significantly influenced by self-trapping and quenching barriers. Rb_2AgCl_3 is identified as having the highest STE emission efficiency, consistent with experimental results. Additionally, by examining the structural compactness, we explain the composition-dependent emission efficiency trends in the Cs_2AgX_3 and Rb_2AgX_3 systems. Our study shows that the excessive electron–phonon coupling strength in 1D Ag(I) halides can be reduced by more compact structures, leading to better emission efficiency. We identify the atomic packing factor as a low-cost, effective descriptor for emission efficiency in Cs_2AgX_3 and Rb_2AgX_3. These findings reveal the complex STE landscape in A_2AgX_3 materials and demonstrate the effectiveness of CCD-based analysis for understanding STE emission efficiency, offering a pathway for designing novel, efficient STE luminescent materials. The identification of the packing factor as a key descriptor provides a new perspective for understanding and optimizing STE emission efficiency in metal halide materials.

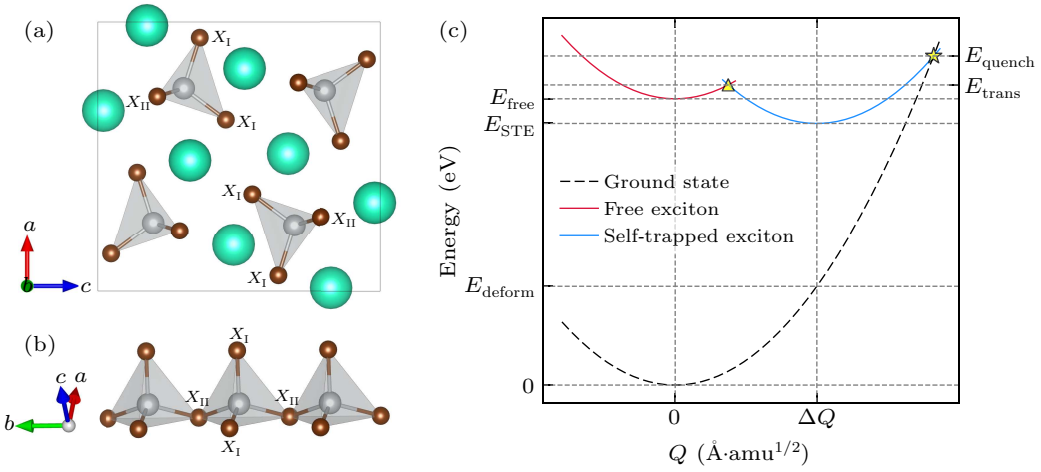


Fig. 1. The 1D crystal structure of A_2AgX_3 (A = Rb, Cs; X = Cl, Br, I) and illustration of STE-CCD. (a) The unit cell viewed from b axis. (b) The X-atom-shared 1D Ag–X atomic chain. Some X atoms are labeled X_I or X_{II}, depending on whether they have one or two coordinating atoms. (c) Schematic of the one-dimensional CCD of STE. The crossing points of the FE-PES and STE-PES, STE-PES and GS-PES are marked by yellow triangle and star, respectively.

2. Computational method

The constrained density functional theory method[36] together with hybrid PBE0 functional,[37,38] which has 25% non-local Fock exchange, is used to study STEs in this work. All calculations were performed under the projector augmented wave (PAW) potential framework implemented in the Vienna *Ab initio* Simulation Package code.[39,40] A kinetic energy cutoff of 400 eV was used for the plane-wave basis. The $1 \times 3 \times 1$ supercell with 72 atoms was used in STE calculations, and lattice parameters were fixed to the experimental values. One gamma point was adopted for the Brillouin zone sampling in STE calculations. Residual forces on atoms converged below 0.01 eV/Å in all ground- and excited-state structure relaxations. The electronic self-consistent field calculations converged with a criterion of 10^{-5} eV/atom. The exciton binding energies were calculated by $\Delta E_{\mathrm{b}} = E\,(\mathrm{GS}) + E_{\mathrm{g}} - E(\mathrm{exciton})$, where $E\,(\mathrm{GS})$ and $E(\mathrm{exciton})$ are the total energies of the ground state and the free exciton state, respectively, and E_{g} is the band gap. The atomic packing factor was calculated by summing the volumes of the atoms within the unit cell and dividing by the volume of the unit cell. The atomic volumes were determined using empirical atomic radii as measured by Slater.[41]

3. Results and discussion

The 1D crystal structure of A_2AgX_3 ($A =$ Rb, Cs; $X =$ Cl, Br, I) is illustrated in Fig. 1(a). In this structure, Ag atoms form tetrahedra with four coordinating halogen atoms, creating a 1D chain by sharing vertices between two tetrahedra. This arrangement allows only two X atoms in each Ag–X tetrahedron to bond with two Ag atoms, while the other two X atoms bond with only one Ag atom. Within one unit cell, the ratio of singly-coordinated X_{I} atoms to doubly-coordinated X_{II} atoms is 2:1. This loose connection makes the structure prone to distortions and renders the Ag–X bonds of the singly-coordinated X atoms highly susceptible to stretching and rotation due to the lack of additional coordination. The proximity of Ag–X chains allows for potential interactions during excited-state structural distortions as well.

Under the PBE functional, these materials exhibit similar electronic structures (Figs. S1 and S2 in supplementary material). The valence band comprises both flat, non-dispersive bands and dispersive bands, indicating charge localization between 1D chains and delocalization within 1D chains. The density of states (DOS) results (Figs. S1 and S2) show that the valence bands are primarily composed of Ag d orbitals and halogen p orbitals, which differs with Cu(I) halides where Cu d orbitals dominate the valence band edge. The conduction band is mainly derived from Ag s orbitals and halogen p orbitals, with a dominance of Ag s orbitals. The DOS shape of Ag s orbitals and halogen p orbitals in the conduction band is consistent, reflecting the strong coupling between these orbitals. Four of the six compounds have direct band gaps at the Γ point, except for Rb_2AgBr_3 and Rb_2AgI_3, which have indirect band gaps only 0.01 eV smaller than the direct gaps at the Γ point. The PBE band gaps range from 2.62 eV to 3.09 eV, decreasing with the increasing atomic number of the halogens and increasing with the atomic number of the alkali metals. Using the PBE0 hybrid functional, the band gap increases by 1.8 eV to 2.2 eV, depending on the halogen species. Specific band gap values are listed in Table S1 of the supplementary material. By comparing the band gaps (free carrier energies) and energies of the free exciton states, both obtained using the PBE0 functional, we determined the exciton binding energies in the A_2AgX_3 system, which range from 0.63 eV to 0.78 eV, as shown in Table S2 of the supplementary material. These relatively large exciton binding energies indicate that free carriers in this system will spontaneously form excitons and are unaffected by thermal fluctuations. The strong Coulomb interaction responsible for this behavior arises from the dimensional confinement of band-edge electrons in the 1D structure, which restricts the spatial distribution of free carriers and promotes exciton formation.

The ground-state electronic structure of the A_2AgX_3 can be summarized by noting that the valence band edge consists of Ag d and X p orbitals, while the conduction band edge consists of Ag s and X p orbitals. Upon excitation, the excited electrons predominantly occupy the Ag s orbitals, and holes occupy the halogen p orbitals. This causes the excited-state electrons to repel the X^- ions and holes repel the Ag^+ ions, resulting in Ag–X bond elongation, which is the dominant form of structural distortion of the STE in 1D Ag(I) halides. The absence of additional bonding constraints makes Ag–X_{I} bonds with 1-coordinated halogen atoms more prone to deformation. Due to the hole occupation of p orbitals, X_{I} atoms may come close to neighboring halogen or Ag atoms to form new X–X or X–Ag bonds, enhancing p–p or p–d hybridization and reducing system energy. These two deformation forms, noted as STE1 and STE2, were successfully identified in all six compounds. Figures 2(a) and 2(b) show the partial charge densities of excited-state electron and hole wave functions in STE1 and STE2 of Cs_2AgBr_3, with results for other materials in supplementary material Figs. S3–S7. In STE1, one Ag–X_{I} bond elongates, allowing the X_{I} atom to approach another X_{I} atom in a neighboring chain, forming a halogen atom pair. The excited-state electron is mainly distributed in the Ag s orbitals of the elongated Ag–X_{I} bond, while the hole is primarily located on the two adjacent halogen atoms and the Ag d orbitals of the neighboring chain. In STE2, the Ag–X_{I} bond elongates and breaks, bringing the X_{I} atom close to the Ag atom of the adjacent chain, forming a new Ag–X bond. The excited-state

electrons in STE2 are mainly on the Ag atom that loses the X atom, while the holes are on the d orbitals of the Ag atom that gains the X atom and on the p orbitals of its ligand halogen atom.

In Cu(I) halides, the primary STE distortion involves two neighboring Cu atoms coming close and forming new Cu–Cu bonds. In 1D Ag(I) halides, the larger interatomic distance between Ag atoms makes it harder for two Ag atoms to approach. However, although this distortion pathway is not the primary mode for STEs in Ag(I) halides, a similar STE state, referred to as STE3, can still be identified in all six compounds. Figure 2(c) shows STE3 in Cs_2AgBr_3, where two Ag atoms in the same chain approach, repelling the X_{II} atom bonded to both Ag atoms and elongating the two Ag–X_{II} bonds. This repelled X_{II} atom may form a halogen atom pair with an X_I atom on a neighboring atomic chain, especially with Br or I, as shown in Fig. 2(c) and supplementary material Figs. S4(c), S6(c), and S7(c). However, if the halogen is Cl, as in Cs_2AgCl_3 and Rb_2AgCl_3, STE3 will not affect neighboring chains, confining structural distortions and excited-state holes to a single atomic chain, as shown in supplementary material Figs. S3(c) and S5(c).

By interpolating between and on both sides of the pristine and STE deformed structures and calculating the ground and excited-state energies, we obtain first-principles CCDs for all 16 STE states in the six compounds, as shown in Fig. 3. These CCDs include the same elements as in Fig. 3, including clearly distinguished FE states and STE states, along with the corresponding transition barriers. Due to computational limitations, we cannot determine the exact intersection of the STE state and the ground state in all CCDs. However, these intersections can be predicted by fitting a harmonic PES function using data points to the right of the STE state, as shown in Fig. S8 in the supplementary material. An important observation is that the self-trapping energy (E_{trap}) of the 16 STE states varies significantly, with many STE states showing negative E_{trap} values, indicating their compromised stability. In Fig. 3, we compare the same type of STEs in three materials, Cs_2AgX_3 (X = Cl, Br, I) and Rb_2AgX_3 (X = Cl, Br, I), to highlight the effect of halogen variation on STEs. It is evident that as the halogen atomic number increases, the degree of structural distortion increases, reflected by the rise in ΔQ. This occurs because as the halogen atomic number increases, the Ag–X bond lengths become longer and the bonding weakens, making the structure more prone to deformation.

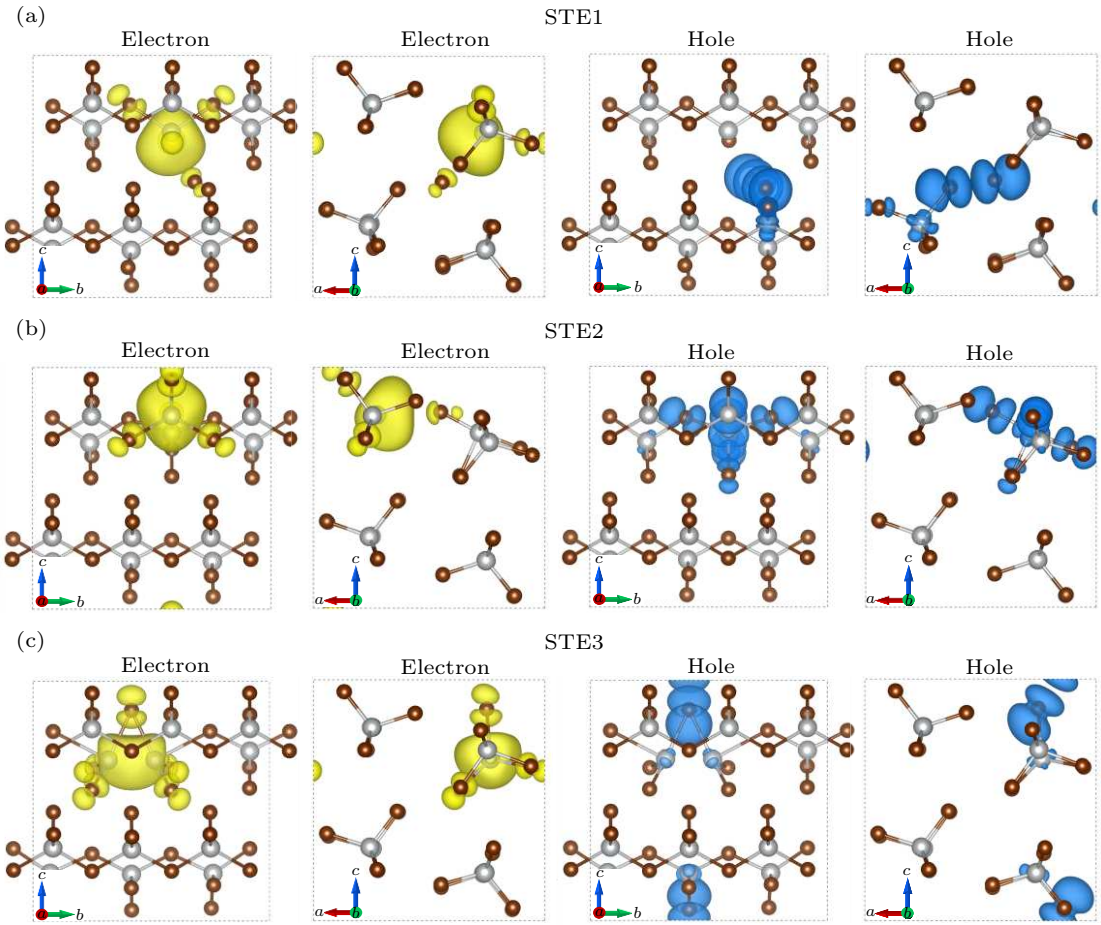


Fig. 2. Partial charge densities of the electron and hole wavefunctions for (a) STE1, (b) STE2, and (c) STE3 in Cs_2AgBr_3, viewed along the a and b axes, with isosurface level set to 0.0008.

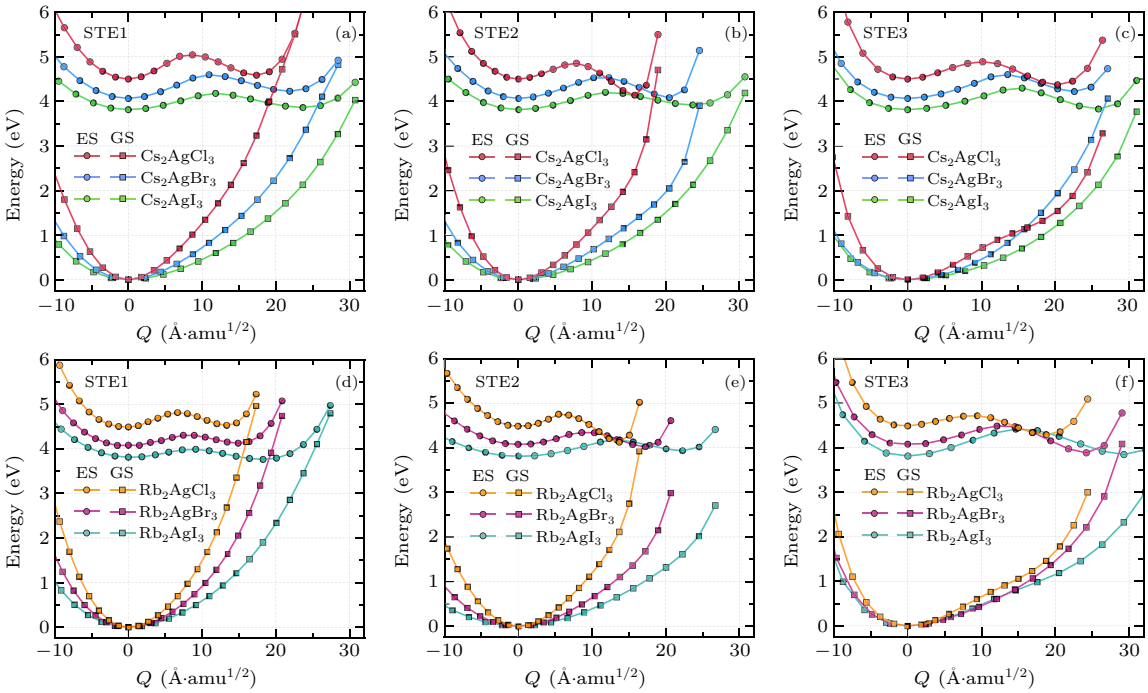


Fig. 3. The calculated CCDs of [(a) and (d)] STE1, [(b) and (e)] STE2 and [(c) and (f)] STE3 in A_2AgX_3 (A = Rb, Cs; X = Cl, Br, I).

We summarize all the ΔQ data in Fig. 4(a) and find that, in addition to a significant increase with the halogen atomic number, there is also a trend of increasing ΔQ with the atomic number of the A-site for the same STE species. This is because a higher atomic number at the A-site increases the atomic volume and cell size, providing more free space within the cell, which enhances the STE distortions. The ΔQ relationship between different STE species depends on the A-site atomic species: STE1 distortions are larger than STE2 distortions in the same material when A = Cs (except for Cs_2AgI_3, where the two STEs are nearly equally distorted), and vice versa when A = Rb. STE3 is the most distorted STE species in all materials because two Ag atoms are involved in the distortion.

All the excitation and emission energies are summarized in Fig. 4(b). The excitation energies show a significant redshift with increasing halogen atomic number, consistent with the redshift observed in the bandgap. The emission energies of different STE species exhibit varying trends: STE1 and STE2 show a slight blue shift or oscillation with increasing halogen atomic number, while STE3 shows a redshift trend. Notably, the STE3 emission energy changes abruptly when the halogen changes from Cl to other halogens, due to the expansion of the STE distortion from a single atomic chain to two neighboring chains.

We also summarize the available experimental spectroscopic results for the six compounds and label the transition energies in Fig. 4(b) and Table S3 of the supplementary material. Overall, the calculated transition energies agree well with the experimental values. The excitation energies match the experimental values and show an identical trend. For emission energies, Cs_2AgI_3 has three experimental measurements with significant differences, and their distribution aligns with the calculated emission energies of the three STEs, suggesting the possibility that all three STEs contribute to the luminescence in this material. For the other five materials, STE2 is the STE species with emission energies that most closely match the experimental values. In the Rb_2AgX_3 (X = Cl, Br, I) system, the emission energies of STE2 precisely match the trend observed in the experimental values, indicating that STE2 may be the primary STE species in these materials.

Until now, the origin of the different emission efficiencies exhibited in the six materials remains unknown. We summarize the PLQY data for the six materials found in the literature in Table 1. This data shows that only three materials, Cs_2AgCl_3, Rb_2AgCl_3, and Rb_2AgBr_3, have measured PLQYs greater than 25%, with the highest value being 60% for Rb_2AgCl_3. In contrast, the maximum PLQY in the other materials did not exceed 21%, with Rb_2AgI_3 having a PLQY of only 0.37%.

Table 1. PLQY data of A_2AgX_3 (A = Rb, Cs; X = Cl, Br, I) from experiment measurements.

Compound	PLQY (%)
Cs_2AgCl_3	28.46,[42] 20,[17] 17[3]
Cs_2AgBr_3	21,[3] 6.37,[4] 1.97[16]
Cs_2AgI_3	14.41,[4] 4.28,[20] $<$ 1[22]
Rb_2AgCl_3	60,[6] 47.87[15]
Rb_2AgBr_3	27,[5] 21.3,[21] 13.9,[23] 1.52[4]
Rb_2AgI_3	0.37[4]

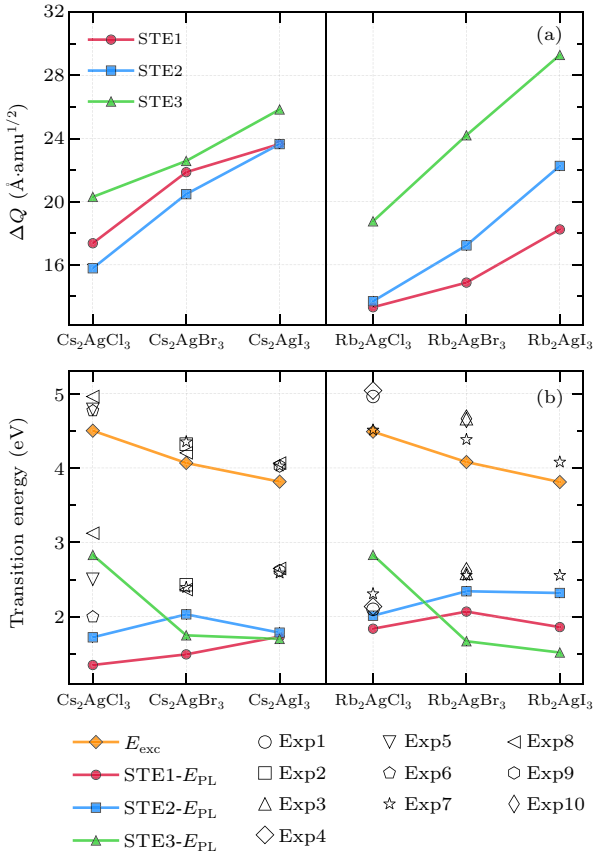


Fig. 4. Trends of (a) ΔQ and (b) optical transition energies in A_2AgX_3 (A = Rb, Cs; X = Cl, Br, I) obtained from their calculated CCDs. The excitation energy (E_{exc}) and emission energy (E_{PL}) obtained from eight experimental references are marked in (b) as well, with higher energy points of the same material to be excitation and lower energy points to be emission. The references corresponding to the experimental work (from Exp1 to Exp10) are as follows: Ref. [15], Ref. [16], Ref. [5], Ref. [6], Ref. [17], Ref. [42], Ref. [23], Ref. [4], Ref. [3], Ref. [20], and Ref. [21].

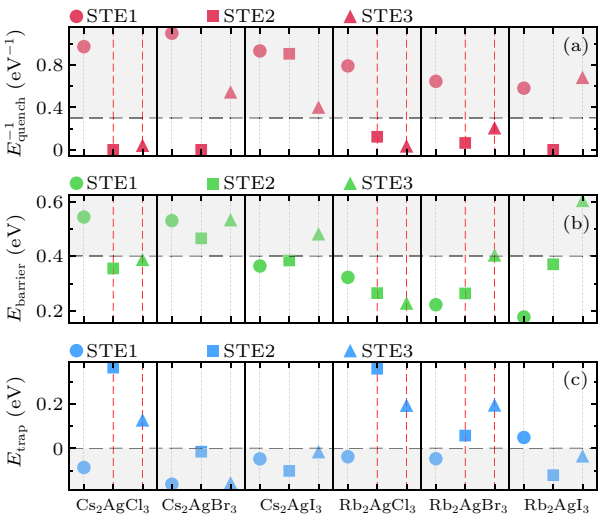


Fig. 5. Screenings of the multiple STEs in A_2AgX_3 (A = Rb, Cs; X = Cl, Br, I) with three distinct criteria obtained from their corresponding CCDs: (a) the inverse of the quenching energy, (b) the self-trapping barrier and (c) the self-trapping energy. The screening thresholds are marked with gray horizontal dashed lines, and the areas to be screened out are covered with light gray shadows. The STEs passed all the screenings are marked out by red vertical lines.

To elucidate the underlying causes of the significant differences in emission efficiency, we compared the self-trapping energy (E_{trap}), self-trapping potential barrier ($E_{barrier}$), and quenching potential barrier (E_{quench}) for all STE states across the six materials, as summarized in Fig. 5. Due to the broad range of E_{quench} values and the absence of intersections for certain STE states, we presented the reciprocal of the quenching potential barriers (E^{-1}_{quench}) in Fig. 5(a), setting E^{-1}_{quench} to 0 for STE states lacking intersections. These three parameters, i.e., E_{trap}, $E_{barrier}$, and E_{quench}, are related to the stability, formability, and quenching probability for emissions of the STE states, respectively, all of which critically influence the emission efficiency. Firstly, as shown in Fig. 5(c), most STE states in these 1D Ag halides have negative self-trapping energies, indicating that they are generally unstable. Only STE2 and STE3 in Cs_2AgCl_3, Rb_2AgCl_3, Rb_2AgBr_3, and STE1 in Rb_2AgI_3 have positive self-trapping energies, meaning that they are more stable than the FE state. Regarding the $E_{barrier}$, as shown in Fig. 5(b), it is generally inversely proportional to the self-trapping energy, indicating that more stable STE states often have lower formation potential barriers. All stable STE states have $E_{barriers}$ below 0.4 eV. For the E^{-1}_{quench}, as shown in Fig. 5(a), stable STE states also have lower E^{-1}_{quench} values (less than 0.3 eV^{-1}), indicating higher quenching potential barriers, except for STE1 in Rb_2AgI_3. Ultimately, STE2 and STE3 in Cs_2AgCl_3, Rb_2AgCl_3, and Rb_2AgBr_3 are identified to have better emission efficiencies, aligning with those having experimental PLQYs greater than 25%. Among them, Rb_2AgCl_3 has the lowest self-trapping barrier, explaining its highest emission efficiency. These results demonstrate that STE emission efficiency in 1D Ag halides can be effectively understood based on complete CCD results from first-principles calculations.

While the CCD provides predictive insights for the STE emission efficiency, it cannot be directly linked to compositional changes in 1D Ag halides. However, experimental results reveal a negative correlation between PLQY and the atomic number of the halogens in both Cs_2AgX_3 (X = Cl, Br, I) and Rb_2AgX_3 (X = Cl, Br, I) systems, and understanding this intriguing trend could enhance our insight into STE luminescence. In Fig. 4(a), we observed a clear linear relationship between ΔQ and halogen composition, with ΔQ increasing linearly as the halogen atomic number rises. This finding prompted us to investigate the connection between ΔQ and emission efficiency. In Fig. 6(a), we plotted the average ΔQ values of the three STEs for each material (ΔQ_{avr}) against the maximum values of experimentally measured PLQY. We found a strong linear negative correlation between PLQY and ΔQ_{avr} in both the Cs_2AgX_3 and Rb_2AgX_3 systems. This suggests that in these two material systems, the excited-state structural deformation, which is linked to electron–phonon coupling, is excessive, so that the reduced ΔQ can help alleviate this issue and improve the efficiency. The dependence

of ΔQ on halogen composition can be attributed to smaller halogen atoms creating more compact structures with stronger bonding, thus reducing deformation. To support this idea, we further explored the relationship between the atomic packing factor and $\Delta Q_{\rm avr}$, as shown in Fig. 6(b). A clear negative linear relationship between the packing factor and $\Delta Q_{\rm avr}$ was observed, confirming that changes in halogen composition can influence excited-state structural deformation by affecting structural compactness. We then examined the relationship between the packing factor and PLQY, as shown in Fig. 6(c), which reveals a strong positive linear relationship in both systems. By summarizing the relationships in Fig. 6, we propose the following mechanism for the compositional dependent trend of STE emission efficiency in 1D Ag(I) halides. Both Cs_2AgX_3 and Rb_2AgX_3 systems generally have loose structures and high electron–phonon coupling strengths, leading to significant excited-state structural deformation and reduced emission efficiency (compared to Cu(I) halides). In this context, smaller halogen atoms result in more compact structures (as reflected by the packing factors) and stronger bonding, which reduces the excited-state structural deformation and enhances the emission efficiency. Notably, we found a perfect positive linear relationship between the packing factor and emission efficiency in both Cs_2AgX_3 and Rb_2AgX_3 systems, which is remarkable because the packing factor can be obtained directly from experimentally measured crystal structures without the need for excited-state or even ground-state first-principles calculations. These findings suggest that the packing factor may serve as an effective and low-cost descriptor for STE emission efficiency in metal halide materials, though further validation in additional material systems is still required.

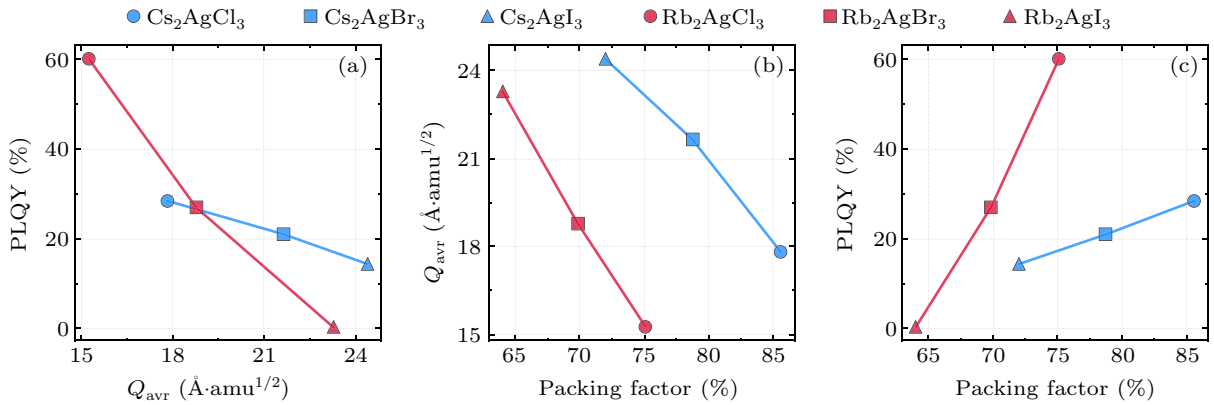


Fig. 6. Trend of compositional dependent STE emission efficiency in 1D Ag halides and its correlation with excited-state structural deformation and ground-state atomic packing factor. (a) $\Delta Q_{\rm avr}$ versus experimentally measured PLQY maxima; (b) stacking factor versus $\Delta Q_{\rm avr}$, and (c) stacking factor versus experimentally measured PLQY maxima.

4. Conclusion

In this study, we investigated the factors influencing STE emission efficiency in the A_2AgX_3 (A = Rb, Cs; X = Cl, Br, I) system. By identifying three distinct STE states in each material and calculating CCDs, we explored the differences in emission efficiency by examining STE stability, self-trapping, and quenching barriers. Additionally, our study highlighted the significant impact of structural compactness on emission efficiency. We demonstrated that excessive electron–phonon coupling, a common issue in 1D Ag(I) halides, can be mitigated by increasing structural compactness, thereby enhancing emission efficiency. The atomic packing factor emerged as a low-cost and effective descriptor for STE emission efficiency in this system, offering a novel perspective on understanding STEs in metal halide materials. These findings deepen our understanding of emission efficiency in metal halides and provide valuable insights for optimizing and designing new high-performance STE-based luminescent materials.

Data availability statement

The data that support the findings of this study, including the structural and partial charge density files of all identified STEs in A_2AgX_3 (A = Rb, Cs; X = Cl, Br, I), are openly available in Science Data Bank at the following link https://doi.org/10.57760/sciencedb.12094.

Acknowledgments

Project supported by the National Natural Science Foundation of China (Grant Nos. 62125402 and 62321166653). Calculations were performed in part at the high-performance computing center of Jilin University.

References

[1] Ma Z, Ji X, Lin S, Chen X, Wu D, Li X, Zhang Y, Shan C, Shi Z and Fang X 2023 *Adv. Mater.* **35** 2300731
[2] Banerjee D and Saparov B 2023 *Chem. Mater.* **35** 3364
[3] Zhang Z, Zhao R, Teng S, Huang K, Zhang L, Wang D, Yang W, Xie R and Pradhan N 2020 *Small* **16** 2004272

[4] Kumar P, Creason T D, Fattal H, Sharma M, Du M H and Saparov B 2021 *Adv. Funct. Mater.* **31** 2104941

[5] Zhang M, Wang X, Yang B, Zhu J, Niu G, Wu H, Yin L, Du X, Niu M, Ge Y, Xie Q, Yan Y and Tang J 2021 *Adv. Funct. Mater.* **31** 2007921

[6] Zhang Z, Guo X, Huang K, Sun X, Li X, Zeng H, Zhu X, Zhang Y and Xie R 2022 *J. Lumin.* **241** 118500

[7] Jun T, Sim K, Iimura S, Sasase M, Kamioka H, Kim J and Hosono H 2018 *Adv. Mater.* **30** 1804547

[8] Zhang Z X, Li C, Lu Y, Tong X W, Liang F X, Zhao X Y, Wu D, Xie C and Luo L B 2019 *J. Phys. Chem. Lett.* **10** 5343

[9] Roccanova R, Yangui A, Seo G, Creason T D, Wu Y, Kim D Y, Du M H and Saparov B 2019 *ACS Mater. Lett.* **1** 459

[10] Creason T D, Yangui A, Roccanova R, Strom A, Du M and Saparov B 2019 *Adv. Opt. Mater.* 1901338

[11] Ma Z, Shi Z, Qin C, Cui M, Yang D, Wang X, Wang L, Ji X, Chen X, Sun J, Wu D, Zhang Y, Li X J, Zhang L and Shan C 2020 *ACS Nano* **14** 4475

[12] Wang L, Shi Z, Ma Z, Yang D, Zhang F, Ji X, Wang M, Chen X, Na G, Chen S, Wu D, Zhang Y, Li X, Zhang L and Shan C 2020 *Nano Lett.* **20** 3568

[13] Ma Z, Shi Z, Yang D, Li Y, Zhang F, Wang L, Chen X, Wu D, Tian Y, Zhang Y, Zhang L, Li X and Shan C 2021 *Adv. Mater.* **33** 2001367

[14] Wang Z, Wang L, Xie J, Yang Y, Song Y, Xiao G, Fu Y, Zhang L, Fang Y, Yang D and Dong Q 2024 *Small* **20** 2309922

[15] Wu D, Luo Y, He P, An K, Lai J, Feng P, Zhou M, Liu Y, Tang X and Han G 2023 *ACS Appl. Opt. Mater.* **1** 78

[16] Fan R, Qiao J, Xu J, Feng S and Liu G 2024 *Opt. Lett.* **49** 3942

[17] Yang D, Wang F, Li S, Shi Z and Li S 2024 *J. Phys. Chem. C* **128** 2223

[18] Yao M M, Zhang Q, Wang D, Chen R, Yin Y C, Xia J, Tang H, Xu W P and Yu S H 2022 *Adv. Funct. Mater.* **32** 2202894

[19] Dai P, Xu Z M and Wang Y X 2011 *Chin. Phys. Lett.* **28** 017804

[20] Fan R, Qiao J, Xu J, Feng S and Liu G 2023 *J. Alloys Compd.* **960** 170858

[21] Wang S, Liu R, Li J, Meng C, Liu J, Chen J, Cheng P and Wu K 2024 *Angew. Chem. Int. Ed.* **63** e202403927

[22] He T, Zhou Y, Wang X, Yin J, Gutiérrez-Arzaluz L, Wang J X, Zhang Y, Bakr O M and Mohammed O F 2022 *ACS Energy Lett.* **7** 2753

[23] Wen X, Buryi M, Babin V, John D, Kučerková R, Nikl M, Wang Q, Li Y, Li W, Yang F, OuYang X and Wu Y 2024 *Laser Photonics Rev.* 2400518

[24] Du M H 2020 *ACS Energy Lett.* **5** 464

[25] Ma Z, Liu Z, Lu S, Wang L, Feng X, Yang D, Wang K, Xiao G, Zhang L, Redfern S A T and Zou B 2018 *Nat. Commun.* **9** 4506

[26] Li Q, Chen Z, Yang B, Tan L, Xu B, Han J, Zhao Y, Tang J and Quan Z 2020 *J. Am. Chem. Soc.* **142** 1786

[27] Dai S, Xing X, Hadjiev V G, Qin Z, Tong T, Yang G, Wang C, Hou L, Deng L, Wang Z, Feng G and Bao J 2023 *Mater. Today Phys.* **30** 100926

[28] Zhang L, Li S, Sun H, Jiang Q, Wang Y, Fang Y, Shi Y, Duan D, Wang K, Jiang H, Sui L, Wu G, Yuan K and Zou B 2023 *Angew. Chem. Int. Ed.* **62** e202301573

[29] Feng Y, Chen Y, Wang L, Wang J, Chang D, Yuan Y, Wu M, Fu R, Zhang L, Wang Q, Wang K, Guo H and Wang L 2024 *Chin. Phys. Lett.* **41** 063201

[30] Stoneham M 2001 *Theories of Defects in Solids* (Oxford, New York: Oxford University Press)

[31] Di Bartolo B 1991 *Advances in Nonradiative Processes in Solids* (Vol. 249) (Boston, MA: Springer US)

[32] Landsberg P T 1992 *Recombination in Semiconductors* (Cambridge: Cambridge University Press)

[33] Jung Y K, Kim S, Kim Y C and Walsh A 2021 *J. Phys. Chem. Lett.* **12** 8447

[34] Xing Z, Zhou Z, Zhong G, Chan C C S, Li Y, Zou X, Halpert J E, Su H and Wong K S 2022 *Adv. Funct. Mater.* **32** 2207638

[35] Wang X, Meng W, Liao W, Wang J, Xiong R G and Yan Y 2019 *J. Phys. Chem. Lett.* **10** 501

[36] Sun H Y, Xiong L and Jiang H 2023 *Chem. Phys. Rev.* **4** 031302

[37] Perdew J P, Ernzerhof M and Burke K 1996 *J. Chem. Phys.* **105** 9982

[38] Adamo C and Barone V 1999 *J. Chem. Phys.* **110** 6158

[39] Kresse G and Furthmüller J 1996 *Phys. Rev. B* **54** 11169

[40] Kresse G and Furthmüller J 1996 *Comput. Mater. Sci.* **6** 15

[41] Slater J C 1964 *J. Chem. Phys.* **41** 3199

[42] Yang C, Wang S, Chen W, Zhang Y, Guo F, Zhou Y, Wang J and Han H 2023 *Chem. Eur. J.* **29** e202301677